

1
2
3
4
5
6
7
8
9
10
11
12
13
14
15
16
17
18
19
20
21
22
23
24
25
26

**Stratified-turbulence observations dominated
by slantwise downward convective warm-
water periods in the deep Mediterranean**

by Hans van Haren

Royal Netherlands Institute for Sea Research (NIOZ), P.O. Box 59, 1790 AB Den Burg,
the Netherlands.
e-mail: hans.van.haren@nioz.nl

27 **Abstract.** A ~~nearly half-cubic hectometer three-dimensional mooring array holding nearly 3000 high-~~
28 ~~resolution temperature sensors in 2500-m³~~ deep Mediterranean-Sea waters is used for a yearlong
29 ~~sampled with about 3000 high-resolution temperature sensors to study on~~ different sources of turbulent
30 waterflows, which are vital for life. Although temperature differences are found never larger than
31 0.01°C, daily, weekly, and seasonal variations are observed. With a delay of about a week, the deep-sea
32 stratified turbulence tracks atmospheric disturbances, which are found 35% more energetic in winter
33 than in summer. About half the time, relatively warm stratified waters are moved to near the seafloor
34 from 100's of meters higher levels ~~to near the seafloor.~~ Combined These internal-wave and sub-
35 mesoscale eddy-induced motions lead to slantwise downward convective warm-water periods that are
36 half an order of magnitude more turbulent than those induced via general geothermal heating from
37 below, and about one order of magnitude more turbulent than those from open-ocean processes. The
38 analysis A rough estimate ~~shows~~ that eddy-induced stratified turbulence is likely more important for deep-
39 sea life than rare, not observed, deep dense-water formation at the abyssal-plain mooring site. ~~With a~~
40 ~~delay of about a week, the stratified turbulence tracks atmospheric disturbances, which are found 35%~~
41 ~~more energetic in winter than in summer. From comparison of turbulence calculation methods, of band-~~
42 ~~pass filtering with vertical displacement reordering, for data over one four days, a generalization is~~
43 ~~proposed for the filter cut offs under weakly stratified and near homogeneous conditions in the deep~~
44 ~~Mediterranean.~~

45

46 1 Introduction

47 Irreversible, energy-consuming turbulence is indispensable for life everywhere on earth, including also
48 in the deep sea. Most ocean turbulence is generated near its boundaries, with an important input via the
49 breaking of internal waves at steeply sloping underwater topography (Eriksen, 1982; Thorpe, 1987).
50 Observational details of turbulence are still scarce from the abyssal deep sea that is commonly
51 considered to be ‘quiescent and stagnant’. One of the key aspects in the breaking of internal waves is
52 the ‘warming phase’, when, e.g., an internal wavetide moves downslope of topography and
53 characteristically (re-)stratifies waters near the seafloor with near-homogeneous waters due to
54 convection turbulence above (van Haren and Gostiaux, 2012). Restratification renders efficient turbulent
55 mixing during the following upslope phase. Indirectly topography-connected are, perhaps less known,
56 are slantwise-moving, warm turbulent waters (van Haren and Dijkstra, 2021). This turbulence
57 generation is possibly related with near-inertial waves and (sub-)mesoscale eddies in basins like the
58 Mediterranean Sea where tides and stratified conditions are both weak. As will be demonstrated in this
59 paper, these warm waters have the potential to generate larger turbulent mixing than in the open-ocean
60 interior.

61 Under weakly stratified conditions, the potential of deep-sea turbulence generation via downward or
62 slantwise moving waters should be compared with local general geothermal heating ‘GH’ through the
63 seafloor (e.g., Pasquale et al., 1996), and with deep dense-water formation ‘DWF’ from the surface (e.g.,
64 Marshall and Schott, 1999). Sparse shipborne microstructure profiling has provided estimates of
65 turbulence contributions from different sources across the Northwestern Mediterranean in which GH
66 geothermal heating is found more important than internal wave breaking (Ferron et al., 2017). However,
67 details of relevant processes are lacking and require high-resolution moored observations over
68 prolonged periods of time.

69 In a stably-stratified environment like the sun-heated ocean, downward motions of warm water
70 reaching the deep seafloor seem impossible and counter-intuitive in relation with irreversible convection
71 turbulence involving motion in three spatial dimensions ‘3D’. Natural, body-forced buoyancy-driven
72 convection (e.g., Dalziel et al., 2008; Ng et al., 2016) applies to denser waters moving down and less
73 dense waters moving up in narrow plumes, i.e. in terms of temperature variations: warmer waters

74 moving up and cooler waters moving down. In the ocean, such buoyancy-driven convection turbulence
75 occurs regularly in the upper O(10) m near the surface during nighttime (e.g., Brainerd and Gregg, 1995)
76 and possibly lower 100 m above the seafloor due to ~~GH geothermal heating~~, depending on the local
77 stratification. It can also occur as ~~DWF deep dense-water formation~~ after specific preconditioning of
78 stratification reduction near the surface in localized areas like polar seas and the Mediterranean during
79 brief irregular, rare periods (Marshall and Schott, 1999). An exemption can occur when ~~salinity~~ ~~the other~~
80 ~~major contributor to density variations~~ dominates over temperature ~~in contributing to density~~ variations:
81 if downward moving warm waters are sufficiently saltier than the ~~irre~~ environment, cooler and fresher
82 waters may move up.

83 A reversible, also 3D, process occurs when internal-wave motions affect the stratified environment
84 (e.g., LeBlond and Mysak, 1978). Such motions may displace relatively warm waters downward during
85 a particular wave-phase, and cooler waters up. However, such displacements will not overturn and
86 vertically mix the different water masses.

87 ~~Nevertheless, an apparent counter-intuitive~~A combination of irreversible and reversible processes
88 was ~~occasionally~~ observed ~~above a slope of Great Meteor Seamount~~ ~~in fresh-water alpine Lake Garda~~,
89 where, in the weakly stratified waters underneath internal waves, convection turbulence was observed
90 ~~(van Haren, 2015). Whilst in those North-Atlantic Ocean waters the effects of salinity could not be~~
91 ~~excluded, confirmation was found in similar observations from fresh-water alpine Lake Garda~~ (van
92 Haren and Dijkstra, 2021). As these observations showed similarity with the warming phase of a
93 nonlinear wave breaking above a sloping seafloor (e.g., van Haren and Gostiaux, 2012), it was suggested
94 that the convection underneath internal waves was either generated via shear moving convection tubes
95 slantwise, or via wave-accelerations overcoming vertical density differences in internal-forcing
96 overcoming reduced gravity, instead of body-forcing overcoming gravity as in natural convection.

97 Similar to the effect of large-scale shear, planetary slantwise convection in the direction of the Earth's
98 rotational vector may be brought about by the horizontal Coriolis parameter f_h (Marshall and Schott,
99 1999). The convection can be induced via resonantly-forced standing inertial waves under homogeneous
100 conditions (McEwan, 1973). At mid-latitudes, apparently-stable stratification having buoyancy

101 frequencies of $N = f_i$, $2f_i$ or $4f_i$ occur in marginal stability due to planetary slantwise convection (van
102 Haren, 2008).

103 In this paper, ~~we further pursue~~ the investigation is further pursued of slantwise downward
104 convective warm-water periods inducing stratified-turbulence that occur frequently in the deep Western
105 Mediterranean. For this purpose, a nearly half-cubic-hectometer large 3D mooring-array is constructed
106 holding about 3000 high-resolution temperature T-sensors and deployed at a 2500-m deep seafloor.
107 Turbulence calculations are made based on Ellison (1957) and Thorpe (1977) overturning scales for a
108 full observational year to investigate potential seasonal variations therein. ~~GOf the~~ governing physics
109 processes that indirectly may affect deep-sea life by inducing or transporting sufficient turbulence for
110 nutrient and oxygen supply are: atmospheric-disturbance generated near-inertial waves, boundary-flow
111 instability generating sub-, $O(1)$ km, and meso-, $O(10-100)$ km, scale eddies. Motions associated with
112 these processes dominate dispersal of water masses in seas and oceans. They are all greatly affected by
113 the rotation of the Earth. ~~While~~ they are however not considered to be part of irreversible ‘small-scale’
114 turbulent mixing, ~~they are all greatly affected by the rotation of the Earth~~. How they transfer energy
115 from the surface to deep-sea small-scales of turbulence dissipation is not yet fully established.

116 The materials and methods are described in Section 2, with an extension of turbulence calculation
117 methods in Appendix A2. The results are presented in Section 3, which starts with a yearlong overview
118 timeseries designating local variations in stratification conditions in comparison with the larger
119 background stratification. The analysis then highlights periods under differently stratified conditions,
120 before presenting yearlong timeseries of turbulence values, their improved statistics and short-scale
121 variations. The various mechanistics and their effects on the deep sea are discussed in Section 4. The
122 large number of independent T-sensors is expected to improve statistics of turbulence values, in an
123 environment where all dynamics is captured by temperature variations of less than 0.01°C . The small
124 temperature variations put a large strain on the technical capabilities of quantifying the deep sea
125 turbulence.

126

127 2 Materials and Methods

128 Sufficiently resolved temperature time series mainly from single mooring lines in well-stratified waters
129 have proven useful for calculating turbulence values (van Haren and Gostiaux, 2012; Cimadoribus et al.,
130 2014) using methods proposed by Ellison (1957) and Thorpe (1977). The original methods need some
131 adaptation to be used in very weakly stratified waters like in the deep Mediterranean Sea. Turbulence
132 values are calculated for dissipation rate of turbulent kinetic energy, henceforth ‘turbulent dissipation
133 rate’, and, for a few instances, turbulent diffusivity.

Formatted: Indent: First line: 0 cm

134

135 **2.1 Sampling network**

Formatted: Font: Bold

136 In order to get some insight in the generation and development of deep-sea turbulence, 2925
137 independent, self-contained high-resolution NIOZ4 temperature ‘T’-sensors were distributed in nearly
138 half-a-million cubic meters of seawater. Details of construction and deployment of the large-ring
139 mooring can be found in van Haren et al. (2021). The large number of independent T-sensors is expected
140 to improve statistics of turbulence values, in an environment where all dynamics is captured by
141 temperature variations of less than 0.01°C. The small temperature variations put a large strain on the
142 technical capabilities of quantifying the deep-sea turbulence.

143 With two supplementary T-sensors registering tilt information above and below, 63 T-sensors were
144 taped at 2-m intervals to 45 vertical lines 125-m tall that each were tensioned to 1.3 kN by a single buoy
145 on top. The T-sensors were located between nominally $h = 1.5\text{-}125.5 \pm 0.5$ m above seafloor and recorded
146 data at a rate of once per 2 s. Three buoys, of lines 1.4, 3.5 and 5.7 (henceforth throughout the text, the
147 original naming ‘group.line’ is shortened without period; for layout see Appendix A1), held a single-
148 point Nortek AquaDopp current meter ~~‘CM’~~ at $h = 126$ m, which recorded data once per 600 s. The lines
149 were attached at 9.5-m horizontal intervals to a steel-cable grid that was tensioned inside a 70-m
150 diameter steel-tube ring functioning as a 140-kN anchor.

151 The ensemble ‘large-ring mooring’ was deployed on the $< 1^\circ$ flat and 2458-m deep seafloor of 42°
152 $49.50'N$, $006^\circ 11.78'E$ just 10 km south of the steep continental slope, 5 km from its abyssal-plain foot,
153 of the Northwestern Mediterranean Sea, in October 2020 (Fig. 1a). At the site’s (mid-)latitude $f_h = 1.08f$.
154 ~~Details of construction and deployment of the large ring mooring can be found in van Haren et al.~~

155 ~~(2021)~~—For calibration and reference purposes, a single shipborne Conductivity Temperature Depth
156 ‘CTD’ profile was obtained to $h = 0.5$ m, about 1 km horizontally from the mooring site during the
157 deployment cruise. Meteorological data were obtained from Island Station ‘Porquerolles’, 43°0’N, 006°
158 12’E.

159 With the aid of Irish Marine Institute Remotely Operated Vehicle ~~(ROV)~~ “Holland I” all 45 vertical
160 lines with T-sensors were successfully recovered in March 2024. Of the lines, 43 were mechanically in
161 good order. Line 18 was hit by the drag parachute, which functioned as a stabiliser during the free-fall
162 deployment, whereby 10 sensors were lost. Line 65 was about 0.5-m lower than nominal because of a
163 loop near the cable grid. Fig. A1 shows the numbering of the lines, which were ordered in six groups
164 for synchronisation purposes. As with previously deployed NIOZ4 T-sensors (for details see van Haren,
165 2018), the individual clocks were synchronised to a single standard clock every 4 hours, so that all T-
166 sensors were sampled within 0.02 s. Line 36 did not register synchronization, possibly due to an electric
167 cable failure. Three T-sensors leaked and <10 were shifted in position due to a tape malfunctioning.
168 After calibration, some 20 extra T-sensors are not further considered due to electronics (noise) problems.
169 In total, 2882 out of 2925 T-sensors functioned as expected for the first 20 months after deployment,
170 with remaining bias due to electronic drift resulting in deviations from absolute accuracy. Depending
171 on the period and type of analysis considered, between 50 and 150 T-sensors showed too large bias
172 requiring additional attention during post-processing of the records from the weakly stratified deep sea.

173 Due to unknown causes all T-sensors switched off unintentionally when the file size on the memory
174 card reached 30 MB. This may have to do with a formatting or programming error. The dataset is ~~it~~
175 implied that a maximum of 20 months long for sensors only registering temperature, and 3 months for
176 those with tilt, though about 2.5-3 years is possible with the present setup of data was obtained.

178 2.2 Post-processing of temperature data

179 With respect to previous NIOZ4 T-sensor version, improvements of the electronics resulted in about
180 ~~twice lower~~ noise levels of 0.00003°C and a doubling in~~twice longer~~ battery life. As described in van
181 Haren (2018), calibration yielded a relative precision of <0.0005±°C, and <0.0001°C after careful post-

Formatted: Font: Bold

Formatted: Indent: First line: 0 cm

182 [processing](#). Bias due to instrumental electronic drift of $< 0.001^{\circ}\text{C mo}^{-1}$ after aging was primarily
183 corrected by referencing daily averaged vertical profiles, which must be stable from a perspective of
184 turbulent overturning in a stratified environment, to a smooth polynomial without instabilities. In
185 addition, because vertical temperature (density) gradients are so small in the deep Mediterranean,
186 reference was made to periods of typically one hour duration that were homogeneous with temperature
187 variations smaller than instrumental noise level (van Haren, 2022). Such periods were on days 350, 453,
188 and 657 in the existing records. This secondary correction included low-pass noise filtering ‘lpf’ of data
189 with time. Under near-homogeneous conditions, a tertiary correction involved lpf of data in the vertical.
190 Temperature records were pressure-corrected by transferring to Conservative Temperature Θ (IOC et

191 al., 2010) using CTD’s mean local salinity value. Henceforth, Θ will be named ‘temperature’, for short.

192

193 **2.3 Turbulence values calculation for different stratification periods**

194 Given the consistent and tight temperature-density relationship (Section 3), corrected temperature data
195 allowed for calculations of turbulence values using the overturning displacement method of Thorpe
196 (1977) by reordering density instabilities. [Details for the method of calculating turbulence values from](#)
197 [moored T-sensor data from well-stratified waters is given in van Haren and Gostiaux \(2012\)](#). Here, the
198 method is applied under weakly stratified conditions in which buoyancy frequency $N \ll 10f$, f denotes
199 the local inertial frequency, [the vertical Coriolis parameter](#). [As the method by Thorpe \(1977\) is typically](#)
200 [applied to profiling data, the vertical spacing of 2 m of moored T-sensors is sufficient to resolve](#)
201 [Ozmidov \(1965\) and largest overturning scales, as has been verified in \(van Haren and Gostiaux, 2012\)](#).
202 [The transition to the energetic turbulence regime occurs for scales \$>1.8\$ m under \$N = f\$ using the](#)
203 [buoyancy-Reynolds number threshold given in \(Gargett et al., 1984\)](#).

204 For the present deep-sea area, distinction is made between periods under environmental conditions
205 when $N \sim f$, somewhat exaggerating named stratified-water ‘SW’ conditions, and $N \ll f$ including
206 unstable values, named near-homogeneous ‘NH’ conditions. For NH, the tertiary correction is needed,
207 and, when unstable overturns exceed the 124-m vertical range of sensors, an extra correction is
208 mandatory because the Thorpe (1977) method of reordering is over-estimating displacements and

Formatted: Font: Bold

Formatted: Indent: First line: 0 cm

209 resulting stratification (van Haren, 2025). Such periods are difficult to trace, because of the extremely
210 small vertical temperature differences, and the selection can only be done manually as it is inadequately
211 automated.

212 For comparison with mean Thorpe (1977) method, turbulence values are also computed using
213 ‘Ellison’-scales (Ellison, 1957 for atmospheric data; Itsweire, 1984 for laboratory data; Moum, 1996 for
214 oceanographic microstructure profiler data). Such scales are determined from moored T-sensor time
215 series by filtering out internal wave and sub-mesoscale motions. The method is quite sensitive for the
216 precise high-pass filter ‘hpf’ cut-off frequency, as was noted for well-stratified Atlantic Ocean waters
217 (Cimatoribus et al., 2014 for oceanographic moored T-sensor data). ~~Here in~~ Appendix A2 ~~proposes~~, a
218 modified version for application to moored T-sensor data under very weakly stratified conditions
219 ~~whereis proposed and~~ filter cut-off frequencies are given for SW and NH conditions in the deep
220 Mediterranean. For both methods, mean values are obtained from moored multiple-line T-sensor records
221 after averaging over at least the largest turbulence scales, over the vertical ‘[...]’, over time ‘<...>’, and
222 over 45 horizontally distributed lines ‘(...)’.

223

224

225

226 **3 Results**

227 **3.1 General yearlong overview and large-scale stratification**

228 The focus is on the first full year of observations to investigate potential seasonal variation in deep-sea
229 turbulence dissipation rate values. The yearlong data-overview time series in Fig. 2 demonstrates 2-30
230 day variations, in waterflow speed (Fig. 2a), temperature (Fig. 2b), horizontal waterflowvelocity
231 difference (Fig. 2c), and vertical temperature difference (Fig. 2d). Such time-variability is typical for
232 sub-meso- and mesoscale motions, which are likely associated with the dynamically unstable,
233 meandering boundary current over the canyon-incised steep continental slope (Crepon et al., 1982) and
234 which may develop into eddies, with strongest flows near the surface and in winter (Albérola et al.,
235 1995; van Haren and Millot, 2003).

236 Over the one year of observations, the deep-sea waterflow speed U seldom exceeds 0.1 m s^{-1} , with
237 little variations through the seasons. U also rather strongly varies with local inertial period, which
238 partially reflects the variable thickness of the graphical curves in Fig. 2a, and which may be understood
239 from comparing the daily-filtered time series with the original one.

240 Inertial motions do not dominate T-sensor data (Fig. 2b,d). Also in contrast with U , the T-data
241 demonstrate a seasonal variation with relatively warmer (Fig. 2b) and more stratified (Fig. 2d) waters in
242 winter, coarsely between days 365 and 495. This seasonal variation is also found in horizontal waterflow
243 difference (Fig. 2c). The entire dynamical temperature variation over the year and up to $h = 125 \text{ m}$ from
244 the seafloor is captured within maximum $|\Delta\Theta| < 0.01^\circ\text{C}$, and commonly amounts only a few
245 millidegrees.

246 About half the time, the temperature difference between $h=1$ and 125 m $\Delta\Theta > 0.0002^\circ\text{C} \equiv T_{\text{thres}}$, a
247 threshold level that is about six times the standard deviation of T-sensor noise level. This temperature
248 difference and which provides an overall stratification resulting in $N > 0.65f$. These relatively warm SW
249 either come from above or from the side, slantwise downward. The other half of the time $\Delta\Theta < T_{\text{thres}}$, N
250 $< 0.65f$ and stratification may be unstable, or NH conditions. Under NH, less than 0.7% of total time
251 negative temperature differences are found exceeding the (absolute value of) threshold level and
252 corresponding with large-scale, $>125\text{-m}$ developed GH geothermal heating. As a result, at the
253 observational site convection turbulence associated with GH geothermal heating is suppressed by warm
254 waters advected into the area most of the time.

255 Although the boundary current is strongest near the surface, it manifests itself at great depths
256 including mesoscale variations at horizontal scales $O(10\text{-}100) \text{ km}$. However, observed spatial waterflow
257 variations over about 50-m horizontally also indicate much smaller-scale, rapidly-fluctuating differences
258 (Fig. 2c). These variations associate, in absolute value, with warm SW conditions in approximately half
259 the cases. No cooling, inversely stratified waters, from above are observed in the yearlong record.

260 Compared to open-ocean waters where large 100-m scale $N > 10f$, the deep Mediterranean SW are
261 characterized by weak stratification with $N = O(f)$. Despite the relatively weak stratification, SW will
262 prove important for turbulent mixing in the area.

263 The single shipborne CTD observations show no dominant influence of salinity over temperature
264 governing density variations, in the lower 500 m above the seafloor (Fig. 3). Over the well-resolved
265 stratified portion between $-2165 < z < -2055$ m, the density-temperature relationship is found to be
266 consistent (cf. van Haren, 2025),

267
$$\delta\sigma_2/\delta\Theta = -0.25 \pm 0.01 \text{ kg m}^{-3} \text{ }^\circ\text{C}^{-1}, \quad \text{---} \quad (1)$$

268 where $\delta\sigma_2$ denotes the density anomaly referenced to a pressure level of 2×10^7 Pa. Hence, Θ can be used
269 as tracer for density variations to quantify turbulent overturning using the Thorpe (1977) [reordering](#)
270 method.

271 In the weakly stratified waters over a vertical range of 100 m, density stratification varies, so that N
272 $< 1f$ or NH is found near the seafloor, and $N \approx 2f$ or SW around $z = -2050$ m (Fig. 3d). Over 25-m
273 vertical ranges, $N \geq 2f$ can be found (Fig. 3d), and over 1-10 m ranges $N > 4f$ may be inferred from Fig.
274 3c around $z = -2110$ and -1980 m. Such thin stratified layers are occasionally also found at greater depths
275 if the better-resolved temperature profile is investigated (Fig. 3b). While the occasional vertical
276 temperature differences of $< 0.01^\circ\text{C}$ in Fig. 2d could result from horizontal differences or fronts, it seems
277 more likely that stratification of around $z = -2050$ m in Fig. 3 is periodically lowered by action from
278 above. Such action is expected down to about $h < 10$ m from the seafloor, a thin layer in which vertical
279 temperature differences are generally very small but not always (black graph in Fig. 2d).

280 Thus, although the moored T-sensors were located between the seafloor and $z = -2332$ m, CTD-
281 measured stratification may vary considerably with depth and time, and physical processes may lower
282 warmer water some 400 m or advecting such waters slantwise, or possibly quasi-horizontally into the
283 range of T-sensors. The precise direction of warm-water motion cannot be determined from single-
284 station profiles, but may be resolved with a properly scaled 3D mooring-array. [First however, details](#)
285 [are investigated from different stratified periods using T-sensors data from a single line.](#)

286
287
288

289 **3.24 1D-details of a [stratifiedn arbitrary warm-water period](#)**

290 Considering an average 5-mK-amplitude warm-water period (cf. Fig. 2b), a 1.3-day depth-time detail
291 from around day 485 is presented from single line 15 (Fig. 4). While waters seem depressed from $h >$
292 125 m, the warming occurs in variable periods of <1 hour (Fig. 4a). During the second half of the
293 warming, 0.001°C additional heat is observed near the top. Relatively warm waters reach the seafloor
294 twice within an inertial period of 0.73 day, around days 485.45 and 485.80. The warming ends with two
295 cooler-water fronts and large overturning reaching the seafloor around day 486.2.

296 The warming is depressed to within $h < 10$ m from the seafloor, with a relatively large vertical
297 temperature gradient between the cooler waters near the seafloor and the warmer waters higher up. This
298 is reflected in the increased value of 2-m-small-scale buoyancy frequency N_s in $h < 30$ m. Turbulent
299 overturns hardly occur between days 485.2 and 486.15 for $h < 5$ m, but are non-negligible in the stratified
300 waters above for $5 < h < 30$ m, and are typically 50-m large ~~farther up~~ for $h > 30$ m (Fig. 4b).

301 Quantifying turbulence dissipation rate requires averaging, over all overturning scales possible, and
302 124-m vertically averaged values demonstrate variations with time over two orders of magnitude, when
303 reordered data are used (Thorpe (1977) method, black graph in Fig. 4c), or using $48 < \omega < 3000$ cpd
304 (cycles per day) band-pass filtered data (Ellison (1957) method cf. Appendix A2, cyan graph in Fig. 4c).

305 Time-depth mean values for line 15 from SW's day 485 are: turbulence dissipation rate $\langle[\epsilon_T]\rangle =$
306 $6 \pm 3 \times 10^{-10} \text{ m}^2 \text{ s}^{-3}$ and turbulent diffusivity $\langle[K_z]\rangle = 1.5 \pm 0.7 \times 10^{-3} \text{ m}^2 \text{ s}^{-1}$ under buoyancy frequency $\langle[N]\rangle$
307 $= 2.9 \pm 0.3 \times 10^{-4} \text{ s}^{-1} \approx 3f$, using Thorpe (1977) method. Modified Ellison (1957)-method $\langle[\epsilon_E]\rangle = 7 \pm 3 \times 10^{-}$
308 $10 \text{ m}^2 \text{ s}^{-3}$ (Appendix A2). There is some bias to low mean turbulence values by disregarding overturns
309 below threshold, which is very low given the $<0.0001^{\circ}\text{C}$ precision of T-sensors after post-processing
310 (van Haren, 2018). However, this bias is well within the error of calculation as turbulence is dominated
311 by the large energy-containing overturns. These mean turbulence values are more than one order of
312 magnitude larger than open-ocean values observed in stratified waters well away from boundaries (e.g.,
313 Gregg, 1989; Polzin et al., 1997; Yasuda et al., 2021).

314

315 **3.32 1D-details of an arbitrary near-homogeneous period**

316 For comparison, such turbulence values are under NH conditions between days 316.5 and 320.5 (Fig.
317 5): $\langle[\epsilon_T]\rangle = 2\pm 1\times 10^{-10} \text{ m}^2\text{s}^{-3}$ and $\langle[K_z]\rangle = 1.1\pm 0.5\times 10^{-2} \text{ m}^2\text{s}^{-1}$ under ~~buoyancy frequency~~ $\langle[N]\rangle =$
318 $0.5\pm 0.2\times 10^{-4} \text{ s}^{-1} = 0.5f$. These values follow partially correcting the original method by Thorpe (1977)
319 for overturns exceeding the height of instrumentation with information from manually selected NH
320 environments that are bounded by stratification above (van Haren, 2025). For periods with NH bounded
321 by stratification above, such as between days 318.6 and 318.96, their mean turbulence dissipation rate
322 is to within 10% the same as found for periods with convection turbulence due to ~~GH~~ geothermal
323 heating: $\epsilon_{GH} = 1.2\times 10^{-10} \text{ m}^2\text{s}^{-3}$. The ϵ_{GH} matches average geophysical heat-flux observations in the area
324 (Pasquale et al., 1996), under the condition that the mixing coefficient of $\Gamma_c = 0.5$ (van Haren, 2025),
325 which is typical for buoyancy-driven convection turbulence (Dalziel et al., 2008). For this period, $\langle[\epsilon_E]\rangle$
326 $= 1.3\pm 1\times 10^{-10} \text{ m}^2\text{s}^{-3}$ (Appendix A2).

327

328 **3.43 Some 45-line statistics of short periods under SW and NH conditions**

329 For consistency and statistics, six half-day periods are considered for computation of turbulence
330 dissipation rate values, three under SW and three under NH conditions. The computations are performed
331 for all 45 vertical lines and averages are computed over the 124-m height and half-day periods. It
332 provides a one-and-a-half order of magnitude distribution of mean turbulence dissipation rate values
333 (Fig. 6).

334 While some values are highly consistent between lines, e.g. the most energetic period on day 441,
335 others show a half-order of magnitude distribution of values like on day 459. Initially, this calculation
336 was set-up to help identify biased T-sensors and the appropriate polynomial correction. After applied
337 tertiary correction, remaining wide distributions are attributed to more general turbulence variability.

338 The statistics certainly improve turbulence dissipation rate values calculated using other
339 instrumentation and methodology, which is generally to within a factor of two at best. The six examples
340 of 45 lines provide about four times better statistics for the half-day periods (Table 1). The three NH
341 values average to $\langle[\epsilon_T]\rangle_{NH} = 1.1\pm 0.2\times 10^{-10} \text{ m}^2\text{s}^{-3}$, which is well within error equivalent to ϵ_{GH} as
342 calculated from heat-flux measurements using for mixing coefficient for convection-turbulence $\Gamma_c = 0.5$

343 (Dalziel et al., 2008), while significantly different from the value for shear-turbulence $\Gamma_{se} = 0.2$ typical
344 for stratified conditions (Osborn, 1980; Oakey, 1982). It thus confirms previous results (van Haren,
345 2025) and laboratory findings for convection-turbulence (e.g., Dalziel et al., 2008). The three SW values
346 average to $\langle[\varepsilon_T]\rangle_{SW} = 8 \pm 5 \times 10^{-10} \text{ m}^2 \text{ s}^{-3}$, noting that the standard deviation_s of individual mean values are
347 one order of magnitude smaller (Table 1).

348 Another consequence of the use of multiple mooring lines besides improved statistics, is some insight
349 in possible distribution of mean turbulence values. While one would expect erratic distribution over the
350 short horizontal distances $<70 \text{ m}$, particularly NH distributions yield two-dimensional consistent images
351 such as on days 459 and 495 (Fig. 7). It provides confidence in consistency of methods used, but results
352 in a puzzling gradient in turbulence that apparently is independent of waterflow (measured at $h = 126$
353 m). For these GH geothermal heating- and near-inertial eddies-dominated periods the 9.5-m interval
354 between lines seems reasonably well chosen, where 100 m may have been too large.

355

356 3.54 Yearlong daily averaged turbulence dissipation rate values for 45 lines

357 A yearlong time series of daily-averaged turbulence values is computed for all 45 lines (Fig. 8). This
358 computation is automated, using a fixed 3rd-order polynomial for primary correction. Since the tertiary
359 correction for $>125\text{-m}$ extending overturns is not applied manually, a criterion for excluding such
360 episodes is usapplied. This criterion is simply based on the daily-averaged temperature difference
361 between uppermost and lowest T-sensor, per line. When $\Delta\Theta < T_{\text{thres}}$, given previously, the daily and
362 vertical mean turbulence dissipation rate is fixed to,

$$363 \quad \langle[\varepsilon_T]\rangle = \varepsilon_{GH} = 1.2 \times 10^{-10} \text{ m}^2 \text{ s}^{-3}, \quad (3)$$

364 the mean value for geothermal heating (van Haren, 2025). This is found to occur ~~in~~ $59 \pm 1.5\%$ of the time,
365 somewhat varying per line, and characterizes NH, besides GH geothermal heating. About $40 \pm 1.5\%$ of
366 the time is characterized by SW.

367 The overall, yearlong, 125-m vertical, and 45-line mean turbulence dissipation rate amounts,

$$368 \quad \langle[\varepsilon_T]\rangle = 2.4 \pm 0.2 \times 10^{-10} \text{ m}^2 \text{ s}^{-3}, \quad (4)$$

369 so that the mean SW turbulence dissipation rate amounts,

370 $\langle \epsilon_T \rangle_{SW} = 4.3 \pm 0.4 \times 10^{-10} \text{ m}^2 \text{ s}^{-3},$ (5)

371 which is thus closely represented by the short periods of days 308 and 485 in Fig. 6, Table 1.

372 Part of the SW-turbulence is attributable to ~~GH geothermal heating~~ in a layer of typically $h = 30 \text{ m}$
373 under stratified waters. This may be inferred from the vertical temperature difference in that layer that
374 passes T_{thres} during only 8% of daily periods, cf. the magenta graph in Fig. 2d. Nevertheless, the
375 advection of warmer waters suppresses ~~GH geothermal heating~~-turbulence, possibly affecting the small-
376 scale distribution in Fig. 7. ~~and~~ The associated 3.5-times larger turbulence dissipation rates (5)
377 ~~compared with geothermal-heating value (3) are mainly generated~~ induced by convection ~~in conjunction~~
378 ~~with and more generally by~~ shear following internal-wave breaking.

379 Considering the yearlong ‘seasonal’ variation that was suggested from the temperature (difference)
380 time series in Fig. 2, and which is represented by the logarithm of daily and vertically averaged $\langle [N] \rangle$
381 in Fig. 8c, the corresponding plot of $\langle \epsilon_T \rangle$ (Fig. 8b) is more difficult to interpret, also in conjunction
382 with meteorological data (Fig. 8a). Different-line data mostly collapse on each other during winter
383 between days 365 and 495, for both $\langle [N] \rangle$ and $\langle \epsilon_T \rangle$. During this period, vertical-line daily mean
384 turbulence dissipation rates most, 27 out of 41, exceed twice the mean value (4), shown by the green
385 asterisks in Fig. 8a. The 11% of time of green-asterisks occurrence average to a mean turbulence
386 dissipation rate of $7 \times 10^{-10} \text{ m}^2 \text{ s}^{-3}$.

387 The average turbulence dissipation rate for the 130-day winter period is 25% higher than the yearlong
388 mean (4). During this period, the wind work $\sim W^2$ is increased by 20% compared to its yearlong average
389 value. A rough visual correspondence is found between $|W|$ (Fig. 8a) and $\lg \langle \epsilon_T \rangle$ (Fig. 8b), the former
390 leading the latter by about one week. The clearest value-collapse of turbulence and stratification data
391 from different lines is found between days 450 and 500. The early-spring period is unlikely governed
392 by deep ~~DWF dense-water formation~~ due to limited meteorological forcing (Fig. 8a), but the preceding
393 winter cooling may induce enhanced sub-mesoscale activity. Although increased sub-mesoscale
394 motions can obscure near-inertial internal waves (van Haren and Millot, 2003), the transfer of energy to
395 internal-wave scales leading to breaking and turbulence is not hampered. Possibly, as near-inertial shear

396 is dominant in well-stratified waters, a shift from shear to convection turbulence may be associated with
397 the increase of sub-mesoscale activity. Such potential energy transfer will be elaborated elsewhere.

398 In contrast, 14% lower mean turbulence dissipation rate than (4) is found during the summer between
399 days 540-670. In this period, W^2 is decreased by 13% compared to its yearlong average value.

400

401

402

403 **4 Discussion and conclusions**

404 The observations show short $O(10)$ day periods of typically 0.005°C warmer waters than their
405 environment appearing from above, but also, as inferred from the 3D mooring-array ([movies in van](#)
406 [Haren et al., 2026](#)), from the sides, [slantwise downward](#). The periods ~~demonstrate~~ [occur at](#) a coarse near-
407 inertial periodicity, which is much less deterministic than a tide, and ~~at~~ twice the inertial periodicity.

408 Like internal waves in the [North-Atlantic Ocean](#) and Lake Garda ([van Haren, 2015](#); van Haren and
409 Dijkstra, 2021), they push stratification to within a few meters from the seafloor. The pushdown is
410 vigorously turbulent, more than one order of magnitude larger than in the open ocean away from
411 boundaries. This relatively large turbulence should not surprise as both the bulk Reynolds number
412 $O(10^6)$ and buoyancy Reynolds number $Re_b = \epsilon/(vN^2) = O(10^4) > 200$ are large, [thereby classifying it as](#)

Formatted: Subscript

413 [energetic regime \(Gargett et al., 1984\)](#), even in the weakly stratified deep sea. The $\nu \approx 10^{-6} \text{ m}^2 \text{ s}^{-1}$ denotes
414 the kinematic viscosity. As ~~GH~~ [geothermal heating](#) is found to be relatively weaker [from below](#), the
415 convection turbulence seems to be driven by the, slanted, internal waves from above.

416 [This slantwise convection turbulence is likely driven via \(sub-\)mesoscale eddies that are reinforced](#)
417 [by atmospheric disturbances \(Fig. 9\). As such they may be compared with deep dense-water formation](#)
418 [from sea-surface to seafloor that may occur over brief periods during a severe winter.](#)

Formatted: Indent: First line: 0,51 cm

419

420 **4.1 Warm-water convection versus hypothetical deep-water formation**

421 While vertical motions by wintertime ~~DWF~~ [deep dense-water formation](#) have been observed via moored
422 observations, [also in the Mediterranean](#) (e.g., Schott et al., 1996), and floats (Steffen and D'Asaro,

Formatted: Indent: First line: 0 cm

423 2002), and surface buoyancy fluxes have been estimated to be $O(10^{-7}) \text{ m}^2 \text{ s}^{-3}$ during convection events
424 (Marshall and Schott, 1999), quantification via observations of turbulence values associated with ~~DWF~~
425 dense-water formation reaching the abyssal seafloor have yet to be made (Thorpe, 2005). Unfortunately,
426 a dense-water event never reached the large-ring mooring while it was underwater. Estimates of deep-
427 convection duration are limited, albeit that some consensus exists about decadal variability or
428 occurrence of seafloor-reaching ~~DWF~~ dense-water formation over a relatively short period of (less than)
429 a week (Lilly et al., 1999), maximum a month, per 8-10 years (Dickson et al., 1996; Mertens and Schott,
430 1998). It is tempting to compare coarse ~~DWF~~ deep dense-water formation turbulence dissipation rate
431 estimates with those GH and SW turbulence calculated from observations at the present mooring site
432 during dominant warm-water convection under SW and geothermal heating under NH.

433 Because of the lack of measurements to quantify ~~DWF~~ deep dense-water formation turbulence, some
434 insight is gained from historic nocturnal convection-turbulence near the ocean surface. Microstructure
435 measurements by, e.g., Brainerd and Gregg (1995) demonstrated turbulence dissipation rate values $>$
436 $10^{-7} \text{ m}^2 \text{ s}^{-3}$ close to the surface and which decreased in the $O(10)$ m near-homogeneous layer to typically,
437 $\varepsilon_{\text{DWF}} \approx 10^{-8} \text{ m}^2 \text{ s}^{-3}$, (6)

438 at a depth just above well-stratified waters below. The one order of magnitude reduced value reflects
439 the erosion of the stratification. Here, we take value (6) as a proxy for turbulence dissipation rate by an
440 event of ~~DWF~~ deep dense-water formation-convection turbulence in waters just above the deep seafloor.

441 In comparison with GH geothermal heating's value (3), ~~DWF~~'s (6) is two orders of magnitude larger.
442 Where GH geothermal heating is quasi-permanent, ~~DWF~~ deep dense-water formation rarely occurs, for
443 example not at all during the presented 20 months of observations. Two orders of magnitude difference
444 implies occurrence of (6) during one month per 8 years to match (3). This is the estimated maximum at
445 a given site.

446 In comparison with atmospheric-enforced mainly sub-mesoscale and internal-wave induced year-
447 average value (4), ~~DWF~~'s (6) would have to occur during 2.5 months per 8 years, or during 9 days every
448 year. This is not observed in the open Liguro-Provençal basin. It implies that, either ~~DWF~~ deep dense-
449 water formation turbulence is stronger than (6) also for $z < -2000$ m, which seems unlikely, or ~~GH~~
450 geothermal heating turbulence and especially SW turbulence are several times, SW turbulence up to one

451 order of magnitude, larger than ~~DWF~~ deep dense-water formation turbulence, when averaged over a
452 decade in time. With their sources of sub-mesoscale eddies and near-inertial waves, the warm SW
453 conditions thus seem more important than ~~DWF~~ deep dense-water formation for supply of fresh
454 materials in the deep-sea area. Recall that the observations are made in an area where tides, normally
455 about half the ocean's mechanical energy source, are weak.

456

Formatted: Indent: First line: 0 cm

457 4.2 A comparison between turbulence from warm-water convection and geothermal heating

458 The observed yearlong mean turbulence dissipation rate value of SW being 2.5 times that of ~~GH~~
459 geothermal heating in the present area is the reverse of findings by Ferron et al. (2017), who find three
460 times larger ~~GH~~ geothermal heating than SW from sparse microstructure profiling across the entire
461 Northwest Mediterranean. The discrepancy may have to do with the location of the large-ring mooring,
462 about 5 km from the foot of the continental slope and most likely regularly located under an eddy or
463 meander of the well-stratified boundary current ~~most of the time~~. These large-scale motions are
464 intensified closer to the sea-surface (Alb rola et al., 1995; van Haren and Millot, 2003).

465 Estimating turbulence dissipation rates from the microstructure profiler plots in Ferron et al. (2017)
466 gives average values for $h = 100\text{-}600$ m (the instruments were stopped some 90 m above the seafloor)
467 of about $2.5 \times 10^{-10} \text{ m}^2 \text{ s}^{-3}$ and $7 \times 10^{-10} \text{ m}^2 \text{ s}^{-3}$, for the Western Mediterranean and specifically Ligurian
468 Sea, respectively. These values are in the same range as mean and SW values (4) and (5), respectively.
469 Both averaged microstructure profiles showed reduction in values in the lower $h = 100\text{-}200$ m to about
470 $1 \times 10^{-10} \text{ m}^2 \text{ s}^{-3}$ and $3 \times 10^{-10} \text{ m}^2 \text{ s}^{-3}$, respectively. For properly processed microstructure profiler data the
471 instrumental error is to within a factor of two for mean turbulence dissipation rate values, not considering
472 environmental variations. The shown values, from the same height above seafloor as the upper range of
473 the moored T-sensors, compare with the ~~GH~~ geothermal heating-(3) and mean-(4) values determined at
474 the large-ring mooring.

475

476 4.3 Mechanistics behind slantwise warm-water convection in the deep sea

477 A contribution of salt to density variations may possibly affect the turbulence values calculated from the
478 moored T-sensors under SW conditions, but density-temperature relationship across stratified layers is

Formatted: Indent: First line: 0 cm

479 found consistent between different years (van Haren, 2025). Also, convection turbulence under SW
480 conditions has been observed in deep alpine-lake Garda where salinity contributes little to density
481 variations (van Haren and Dijkstra, 2021).

482 The relative importance of stratified turbulence occurring in varying strength over about half the time
483 has consequences for deep-sea transport, redistribution of matter, and life. The regular replenishment is
484 partially related with atmospheric disturbances, in an indirect way. Winds do not directly affect motions
485 near the 2500-m deep seafloor. However, wind-induced near-inertial internal waves and boundary-
486 current variations affecting sub-mesoscale eddies seem to have correspondence with turbulence intensity
487 variations close to the seafloor, roughly a week after variations occur near the surface. More SW activity
488 and about 20% larger turbulence dissipation rates were found in winter when atmospheric activity was
489 correspondingly larger. Weakest stratification was found more in summer. As eddies and near-inertial
490 waves cause convection in the direction of the rotational axis to slant to the vertical under weak z-
491 direction stratification $N = O(f)$, cf. McEwan (1973); Straneo et al. (2002); Sheremet (2004); Gerkema
492 et al. (2008), the stratified turbulence may come from above and in part horizontally.

493 Mesoscale anticyclonic eddies in the central Mediterranean show observed downward vertical
494 motions along their rim (van Haren et al., 2006). Such eddies may trap and tunnel near-inertial waves
495 (Kunze, 1985), providing different internal wave behavior in the eddy's rim and core (Fig. 9).

496 Comparing periods under SW and NH conditions, deep-sea temperature variance is much larger at
497 all frequencies under SW, but a distinct spectral peak is lacking (Fig. A2). Temperature variations are
498 not governed by quasi-deterministic signals like near-inertial motions, but predominantly by sub-
499 mesoscale and turbulence motions. At most, a bulge is found near the buoyancy frequency in open-
500 ocean displacement spectra (Munk, 1980). For both the open ocean and the Mediterranean Sea, this
501 contrasts with waterflow kinetic energy spectra that show a near-inertial peak. In the deep Mediterranean
502 poorly resolved waterflow measurements such a peak is observed mainly under NH conditions, while
503 kinetic energy is higher at all other frequencies, especially at sub-inertial frequencies, under SW
504 conditions.

505 Thus, under SW all near-inertial motions are feeding, or are overwhelmed by, sub- and super-inertial
506 motions, which results in the continuous slope in temperature spectra with a plateau in the inertio-gravity

507 wave band, up to about the maximum small-scale buoyancy frequency. The wider inertio-gravity wave
508 band under NH sees more temperature variance near its bounds.

509 In between stratified turbulence periods, waters tend to become near-homogeneous whilst being
510 dominantly mixed by convection turbulence through GH geothermal heating. As in Rayleigh-Taylor
511 convection, plumes of GH geothermal heating-response in waters overlying the seafloor strongly vary
512 with time, and thus spatially (e.g., Dalziel et al. 2008; Ng et al., 2016).

513 Geologically, even over a nearly flat sedimented seafloor underlying crustal cracks may develop
514 variable GH geothermal heating over distances as small as <1 km, depending on location of faults (e.g.,
515 Kunath et al., 2021). This could explain observed variation in mean turbulence dissipation rates over the
516 70-m size of the large-ring mooring, during GH geothermal heating. The 0.6-m high steel tubes of the
517 large ring will not affect GH geothermal heating up to $h = 125$ m. An inconclusive variation of mean
518 turbulence values over periods of SW conditions demonstrates larger scale variability.

519 Overall, the 45 vertical lines and nearly 3000 high-resolution T-sensors provided improved statistics
520 for daily mean turbulence dissipation rate values to within a reduced relative error of about 25%. Other
521 strengths of the mooring-array like improved spectral resolution and 3D evolution of turbulence will be
522 reported elsewhere, while short movies of 3D turbulence passages have been described in van Haren et
523 al. (2026).

524 The deep Mediterranean Sea observations are likely general for the deep ocean above a flat seafloor,
525 in the vicinity of large topography. This is because (sub-)mesoscale eddies, inertial motions and
526 geothermal heating are generally occurring. However, as tides and stratification are relatively weak in
527 the Mediterranean, compared to similar depths in the ocean, the observed turbulence processes may be
528 more difficult to detect in the ocean.

529
530 *Data availability.* Only raw data are stored from the T-sensor mooring-array. Analyses proceed via
531 extensive post-processing, including manual checks, which are adapted to the specific analysis task.
532 Because of the complex processing the raw data from the custom-made T-sensors are not made publicly
533 accessible. Current meter and CTD data are available from van Haren (2025): “Large-ring mooring

534 current meter and CTD data”, Mendeley Data, V1, <https://doi.org/10.17632/f8kfwcvtdn.1>. Atmospheric
535 data are retrieved from <https://content.meteoblue.com/en/business-solutions/weather-apis/dataset-api>.

536

537 *Competing interests.* The author has no competing interests.

538

539 *Acknowledgments.* This research was supported in part by NWO, the Netherlands organization for the
540 advancement of science. Captains and crews of R/V Pelagia are thanked for the very pleasant
541 cooperation. NIOZ colleagues notably from the NMF department are especially thanked for their
542 indispensable contributions during the long preparatory and construction phases to make this unique
543 sea-operation successful. I am indebted to colleagues in the KM3NeT Collaboration, who demonstrated
544 the feasibility of deployment of large three-dimensional deep-sea research infrastructures. E. Berbee, P.
545 Kooijman, E. de Wolf, and E. Koffeman showed steep learning curves.

546

547 **Appendix A1 Layout of large-ring mooring**

548 The large-ring mooring has a diameter of nearly 70 m (Fig. A1). The eighteen 12-m long and 0.6-m
549 diameter steel tubes hold a steel-cable grid for rigidity. The cables are 9.5 m apart. At cable-intersects,
550 2.5-m diameter 'small' rings are mounted that each held a 125-m long mooring line with 65 T-sensors
551 below a single 1.45-kN buoy. Of eight small rings, imaginary intersects were at the steel tubes, so that
552 special off-set mounting was needed with three assist cables (van Haren et al., 2021). Upon landing at
553 the seafloor following parachute-controlled 'free' fall, the orientation of the ring was directed to the
554 ~~north-northwest~~ **NNW**, pointing at 337 °N. After underwater chemical release of the buoys, the cable-
555 grid was lifted in a dome with its center h = 2.0 m above seafloor (van Haren, 2026 submitted).

556 The vertical mooring lines were named in six synchronisation groups, of maximum eight lines each.
557 The single synchroniser was located at the small ring of central line 51. Every half hour, the synchroniser
558 sent a clock pulse to a group. The synchronisation sequence of six pulses was repeated every four hours.
559

560 **Appendix A2 Proposed generalization of filter cut-off to compute Ellison scales**

561 Data from moored strings of high-resolution temperature sensors are potentially useful to compare two
562 different manners of calculating turbulence values. The more common method proposed by Thorpe
563 (1977) involves the reordering or sorting of unstable density overturns and the bookkeeping of their
564 vertical displacements, for vertical profiles at each time step. Turbulence values are computed following
565 averaging in the vertical, in time, or both and should include the largest of overturn scales. The method
566 requires a consistent temperature-density relationship. In near-homogeneous waters, difficulties may
567 arise in establishing such a relationship, but also in determining the size of largest overturns when they
568 outgrow the height of the string. A method is proposed to correct over-estimation under convection
569 turbulence by ~~GH geothermal heating~~ using verification via results from geophysical sampling (van
570 Haren, 2025).

571 In well stratified waters, the Thorpe (1977) method has been successfully compared (e.g., Itsweire,
572 1984; Moum, 1996; Cimattorus et al., 2014), with results from the method introduced for atmospheric
573 data by Ellison (1957). In this Appendix, such a comparison is done for weakly stratified waters. A
574 modification is proposed of the Ellison (1957) method for application to data from moored instrumented
575 strings, and which is practically based on instrument performance and environmental physics conditions.

576 Ellison (1957) separated time series of potential temperature $\theta(t, z)$, which is dynamically equivalent
577 to Conservative Temperature Θ (IOC et al., 2010) in the ocean, at a fixed vertical position z in two,

578
$$\theta = \langle \theta \rangle + \theta', \tag{A1}$$

579 where $\langle \cdot \rangle$ denotes the lpf series and the prime its hpf equivalent. If multiple sensors are deployed in the
580 vertical to establish a mean vertical gradient, a scale height can be defined as,

581
$$L_E = \langle \theta'^2 \rangle^{1/2} / (d\langle \theta \rangle / dz). \tag{A2}$$

582 Itsweire (1984), using laboratory CTD-profile data, and Moum (1996), using ocean microstructure
583 profiler data, apply sorting as filter in z -direction. While their quasi-hpf data unlikely contain (linear)
584 internal waves, provided the profiles were instantaneously made and strictly vertical, they may contain
585 instrumental noise. With limited time-evolution available, it is assumed that the hpf data have worked

Formatted: Indent: First line: 0,51 cm

586 against the local stratification. The same assumption is made for Thorpe (1977) displacements. Sorting
587 works on all scales of overturns, which can be highly varying.

588 Like Thorpe-displacement ‘d’ scales, the Ellison scales of (A2) may be compared with the Ozmidov
589 (1965) scale $L_O = cL_E$ of largest possible turbulent overturns in stratified waters, so that the turbulence
590 dissipation rate reads,

$$591 \quad \varepsilon_E = c^2 L_E^2 N^3, \quad (A3)$$

592 in which the constant c needs to be established. If we take an average value of $c = 0.8$ (Dillon, 1982),
593 like commonly used for vertical root-mean-square ‘rms’ Thorpe scale $L_T = [d^2]^{1/2}$ so that $\varepsilon_T = c^2 L_T^2 N^3$,
594 one can compare average [turbulence](#) dissipation rate values between the two methods.

595 While the Thorpe (1977) method is most sensitive to proper resolution of the largest vertical overturn
596 scale, and the stratification (or buoyancy frequency) it works against, determination of Ellison scales
597 from moored-sensor time series is most sensitive for the appropriate separation between internal waves
598 and turbulent motions (Cimatoribus et al., 2014). For data from instrumented strings under well-
599 stratified Northeast-Atlantic conditions, wavelet decomposition worked using an averaging scale of
600 about $2/N$ for the lpf in (A1). Under such conditions, instrumental flaws like short-term bias of T-sensor
601 data were minimal. However, such a determination of Ellison scales is not a straightforward task under
602 weakly stratified and near-homogeneous conditions like occurring in the deep Western Mediterranean.

603 First, because such conditions imply very small variations in temperature (density), time series
604 require lpf to remove instrumental noise.

605 Second, time series require hpf to remove internal waves and (sub-)mesoscale motions. While the
606 common internal-wave band is considered between ranges f and N , for well stratified waters $N \gg f$,
607 more complex inertio-gravity wave [IGW](#) frequency ‘ ω ’ bounds [$\omega_{\min} < f$, $\omega_{\max} > N$], for large-scale mean
608 N , have to be considered in waters where $N = O(f)$, e.g. (LeBlond and Mysak, 1978; Gerkema et al.,
609 2008). Furthermore, while average large-scale stratification hampers turbulent overturns, internal-wave
610 straining separates small thin-layer stratification, with small-vertical-scale buoyancy frequency N_s , from
611 near-homogeneous layers, with minimum buoyancy frequency N_{\min} , which may carry ditto waves
612 extending beyond the mean- N [IGW inertio-gravity wave](#)-bounds. At the low-frequency, sub-inertial

613 side of the ~~IGW~~ inertio-gravity wave-band the rare N_{\min} may combine with sub-mesoscale motions.
614 More importantly, at the high-frequency, super-buoyancy side N_s may combine with turbulent overturns.
615 If all relevant scales are resolved, a safe separation frequency would thus be at overall maximum N_{\max}
616 $= \max(\max(N_s))$, where the maximum between brackets is determined for each profile. In practice, such
617 a transition frequency between internal waves and turbulence is not easily determined, because it
618 requires the small scales to resolve relevant L_o . Only in weakly stratified waters, L_o are $O(10)$ m, and
619 resolution of 1-2 m scales should be sufficient.

620 Thus, under weakly stratified conditions, instrumental noise and short-term bias have to be corrected
621 in t- and z-direction, respectively. A practical solution that also eliminates internal waves and sub-
622 mesoscale motions, is application of a band-pass filter 'bpf' in t, an lpf and sorting in z so that per time
623 step (A2) reads,

$$624 \quad |\theta'_{\text{bpf}}| / (d\theta_{\text{sorted}}/dz),$$

625 to which sufficient averaging is applied. Noting that stratification varies over different scales by two
626 orders of magnitude, so that $N_s \approx 0-6f$, filter design discriminates between conditions of SW and NH.
627 Sharp, phase-preserving double-elliptic filters (Parks and Burrus, 1987) are designed following
628 inspection of temperature variance spectra (Fig. A2).

629 For SW, reasonable filter cut-offs are tuned for a 1.7-day period around day 308 by equating (A3) to
630 ϵ_T . SW's lpf cut-off is fixed at 3000 cpd. The reference hpf cut-off frequency $\omega_{\text{hpf,ref}}$ appeared at a small
631 flat (0-)slope near the low end of turbulence buoyancy- $(\omega^{-7/5})$ and inertial-subrange $(\omega^{-5/3})$ slopes, where
632 a short steep slope to internal-wave frequencies occurred. For other SW-periods, reference is not made
633 using average large-scale N , but a better fit is found for the time average of maximum small-scale
634 buoyancy frequencies per profile $N_m = \langle \max(N_s) \rangle$ so that,

$$635 \quad \omega_{\text{hpf}}^{\text{SW}} = (N_m / N_{m,\text{ref}})^2 \omega_{\text{hpf,ref}}. \quad (\text{A4})$$

636 For NH, the lpf cut-off is fixed at 500 cpd. For its hpf cut-off, a flat (0-) slope appeared at a frequency
637 just higher than ω_{max} so that, independent of measured $\langle N_{s,\text{max}} \rangle$ the cut-off is blocked at,

$$638 \quad \omega_{\text{hpf}}^{\text{NH}} = 3.7 \text{ cpd}. \quad (\text{A5})$$

639 This value is tuned for a period with dominant GH geothermal heating, for which the geophysics-
640 determined (e.g., Pasquale et al., 1996) buoyancy flux $f/\Gamma_c = \varepsilon_{GH} = 1.2 \times 10^{-10} \text{ m}^2 \text{ s}^{-3}$. In the present (Fig.
641 6) and previous (van Haren, 2025) data the mixing coefficient was found to amount $\Gamma_c = 0.5$, which is
642 typical for convection turbulence (Dalziel et al., 2008; Ng et al., 2016).

643 The cut-off frequency in (A5) is to within ± 0.2 cpd equivalent to $1.8(2\Omega) \approx 1.8\langle\omega_{\max}\rangle \approx 2\langle N_{s,\max}\rangle$
644 $\approx 0.5\langle U\rangle/\langle L_T\rangle = 0.5\omega_o$, for the deep Western Mediterranean site. Ω denotes the Earth rotation, and U
645 the waterflow speed. The Ozmidov (1965) frequency ω_o is a natural separator between internal waves
646 and stratified turbulence. It is unknown why the filter cut-off is close to half the Ozmidov frequency.
647 Also puzzling is the lack of correspondence between (A4) and ω_o , with the factor varying between 0.3
648 and 0.9 for different periods of SW. In part this may have to do with the waterflow being measured at h
649 = 126 m, below which it may be more uniform under NH- than under SW-conditions.

650 As shown in Fig. 4 for (A4), and Fig. 5 for (A5), the comparison between average turbulence
651 dissipation rate values using Ellison (1957) and Thorpe (1977) methods works well to within a relative
652 error of about 20% of the mean value. ~~To For~~ Fig. 4, $\langle[\varepsilon_T]\rangle = 6.3 \times 10^{-10} \text{ m}^2 \text{ s}^{-3}$ and $\langle[\varepsilon_E]\rangle = 6.7 \times 10^{-10} \text{ m}^2$
653 s^{-3} . ~~To For~~ Fig. 5, $\langle[\varepsilon_T]\rangle = 2.0 \times 10^{-10} \text{ m}^2 \text{ s}^{-3}$ and $\langle[\varepsilon_E]\rangle = 1.3 \times 10^{-10} \text{ m}^2 \text{ s}^{-3}$. Further tests were performed
654 for about ten 1-4 day periods of NH and SW, and all were within above relative error, provided that the
655 data post-processing was carefully done and longer periods were avoided. Especially (A5) is very
656 sensitive to small changes in filter steepness around the cut-off frequency, presumably due to its
657 proximity to the IGW inertio-gravity wave upper bound.

658

659 **References**

- 660 Adrián-Martinez, S. et al.: Letter of intent for KM3NeT 2.0, *J. Phys. G*, 43, 084001, 2016.
- 661 [Albérola, C. Millot, C., and Font, J.: On the seasonal and mesoscale variabilities of the Northern Current](#)
662 [during the PRIMO-0 experiment in the western Mediterranean Sea, *Oceanol. Acta*, 18, 163-192,](#)
663 [1995.](#)
- 664 Brainerd, K. E., and Gregg, M. C.: Surface mixed and mixing layer depths, *Deep-Sea Res. I*, 42, 1521-
665 1543, 1995.
- 666 Cimadoribus, A. A., van Haren, H., and Gostiaux, L.: Comparison of Ellison and Thorpe scales from
667 Eulerian ocean temperature observations, *J. Geophys. Res.*, 119, 7047-7065, 2014.
- 668 Crepon, M., Wald, L., and Monget, J. M.: Low frequency waves in the Ligurian Sea during December
669 1977, *J. Geophys. Res.*, 87, 595-600, 1982.
- 670 Dalziel, S. B., Patterson, M. D., Caulfield, C. P., and Coomaraswamy, I. A.: Mixing efficiency in high-
671 aspect-ratio Rayleigh-Taylor experiments, *Phys. Fluids*, 20, 065106, 2008.
- 672 Dickson, R. R., Lazier, J. R. N., Meincke, J., Rhines, P., and Swift, J.: Longterm coordinated changes
673 in the convective activity of the North Atlantic, *Progr. Oceanogr.*, 38, 241-295, 1996.
- 674 Dillon, T. M.: Vertical overturns: a comparison of Thorpe and Ozmidov length scales, *J. Geophys. Res.*
675 87, 9601-9613, 1982.
- 676 Ellison, T. H.: Turbulent transport of heat and momentum from an infinite rough plane, *J. Fluid Mech.*,
677 2, 456-466, 1957.
- 678 Eriksen, C. C.: Observations of internal wave refraction of sloping bottoms, *J. Geophys. Res.*, 87, 525-
679 538, 1982.
- 680 Ferron, B., Bouruet Aubertot, P., Cuypers, Y., Schroeder, K., and Borghini, M.: How important are
681 diapycnal mixing and geothermal heating for the deep circulation of the Western
682 Mediterranean? *Geophys. Res. Lett.*, 44, 7845-7854, 2017.
- 683 [Gargett, A. E., Osborn, T. R., and Nasmyth, P. R.: Local isotropy and the decay of turbulence in a](#)
684 [stratified fluid, *J. Fluid Mech.*, 144, 231-280, 1984.](#)
- 685 Gerkema, T., Zimmerman, J. T. F., Maas, L. R. M., and van Haren, H.: Geophysical and astrophysical
686 fluid dynamics beyond the traditional approximation, *Rev. Geophys.*, 46, RG2004, 2008.

687 Gregg, M. C.: Scaling turbulent dissipation in the thermocline, *J. Geophys. Res.*, 94, 9686-9698, 1989.

688 IOC, SCOR, and IAPSO: The International Thermodynamic Equation of Seawater – 2010: Calculation
689 and Use of Thermodynamic Properties, Intergovernmental Oceanographic Commission,
690 Manuals and Guides No. 56, UNESCO, Paris, 196 pp, 2010.

691 Itsweire, E. C.: Measurements of vertical overturns in a stably stratified turbulent flow, *Phys. Fluids*,
692 27, 764-766, 1984.

693 Kunath, P., Chi, W.-C., Berndt, C., and Liu, C.-S.: A rapid numerical method to constrain 2D focused
694 fluid flow rates along convergent margins using dense BSR-based temperature field data, *J.*
695 *Geol. Res. Solid Earth*, 126, e2021JB021668, 2021.

696 Kunze, E.: Near-inertial wave propagation in geostrophic shear, *J. Phys. Oceanogr.*, 15, 544-565, 1985.

697 LeBlond, P. H., and Mysak, L. A.: *Waves in the Ocean*, Elsevier, New York, 602 pp, 1978.

698 Lilly, J. M., Rhines, P. B., Visbeck, M., Davis, R., Lazier, J. R. N., Schott, F., and Farmer, D.: Observing
699 Deep Convection in the Labrador Sea during Winter 1994/95, *J. Phys. Oceanogr.*, 29, 2065-
700 2098, 1999.

701 Marshall, J., and Schott, F.: Open-ocean convection: Observations, theory, and models, *Rev. Geophys.*
702 37, 1-64, 1999.

703 McEwan, A. D.: A laboratory demonstration of angular momentum mixing, *Geophys. Fluid Dyn.*, 5,
704 283-311, 1973.

705 Mertens, C., and Schott, F.: Interannual Variability of Deep-Water Formation in the Northwestern
706 Mediterranean, *J. Phys. Oceanogr.*, 28, 1410-1424, 1998.

707 Moum, J. N.: Energy-containing scales of turbulence in the ocean thermocline, *J. Geophys. Res.*, 101,
708 14,095-14,109, 1996.

709 Munk, W. H.: Internal wave spectra at the buoyant and inertial frequencies, *J. Phys. Oceanogr.* 10, 1718-
710 1728, 1980.

711 Ng, C. S., Ooi, A., and Chung, D.: Potential energy in vertical natural convection, Proc. 20th
712 Australasian Fluid Mech. Conf., Paper 727, 4 pp.,
713 [https://people.eng.unimelb.edu.au/imarusic/proceedings/20/727 Paper.pdf](https://people.eng.unimelb.edu.au/imarusic/proceedings/20/727%20Paper.pdf), 2016.

Formatted: Font: Not Italic

Formatted: Font: Not Italic

Formatted: No underline, Font colour: Auto

Formatted: No underline, Font colour: Auto

Field Code Changed

714 Oakey, N. S.: Determination of the rate of dissipation of turbulent energy from simultaneous temperature
715 and velocity shear microstructure measurements, *J. Phys. Oceanogr.*, 12, 256-271, 1982.

716 Osborn, T. R.: Estimates of the local rate of vertical diffusion from dissipation measurements, *J. Phys.*
717 *Oceanogr.* 10, 83-89, 1980.

718 Ozmidov, R. V.: About some peculiarities of the energy spectrum of oceanic turbulence, *Dokl. Akad.*
719 *Nauk SSSR*, 161, 828-831, 1965.

720 Parks, T. W., and Burrus, C. S.: *Digital Filter Design*, John Wiley Sons, New York, 342 pp, 1987.

721 Pasquale, V., Verdoya, M., and Chiozzi, P.: Heat flux and timing of the drifting stage in the Ligurian–
722 Provençal basin (northwestern Mediterranean), *J. Geodyn.*, 21, 205-222, 1996.

723 Polzin, K. L., Toole, J. M., Ledwell, J. R., and Schmitt, R. W.: Spatial variability of turbulent mixing in
724 the abyssal ocean, *Science*, 276, 93-96, 1997.

725 Schott, F., Visbeck, M., Send, U., Fischer, J., Stramma, L., and Desaubies, Y.: Observations of deep
726 convection in the Gulf of Lions, northern Mediterranean, during the winter of 1991/ 92, *J. Phys.*
727 *Oceanogr.*, 26, 505-524, 1996.

728 Sheremet, V. A.: Laboratory experiments with tilted convective plumes on a centrifuge: A finite angle
729 between the buoyancy force and the axis of rotation, *J. Fluid Mech.*, 506, 217-244, 2004.

730 Steffen, E. L., and D’Asaro, E.: Deep convection in the Labrador Sea as observed by Lagrangian floats,
731 *J. Phys. Oceanogr.*, 32, 475-492, 2002.

732 Straneo, F., Kawase, M., and Riser, S. C.: Idealized models of slantwise convection in a baroclinic flow,
733 *J. Phys. Oceanogr.*, 32, 558-572, 2002.

734 Thorpe, S. A.: Turbulence and mixing in a Scottish loch, *Phil. Trans. Roy. Soc. Lond. A*, 286, 125-181,
735 1977.

736 Thorpe, S. A.: Current and temperature variability on the continental slope, *Phil. Trans. Roy. Soc. Lond.*
737 *A*, 323, 471-517, 1987.

738 Thorpe, S. A.: *The turbulent ocean*, Cambridge Univ Press, Cambridge, 439 pp, 2005.

739 van Haren, H.: Abrupt transitions between gyroscopic and internal gravity waves: the mid-latitude case,
740 *J. Fluid Mech.*, 598, 67-80, 2008.

741 [van Haren, H.: Instability observations associated with wave breaking in the stable-stratified deep-](#)
742 [ocean, Phys. D, 292-293, 62-69, 2015.](#)

743 van Haren, H.: Philosophy and application of high-resolution temperature sensors for stratified waters,
744 Sensors, 18, 3184, doi:10.3390/s18103184, 2018.

745 van Haren, H.: Thermistor string corrections in data from very weakly stratified deep-ocean waters,
746 Deep-Sea Res. I, 189, 103870, 2022.

747 van Haren, H.: Corrected values of turbulence generated by general geothermal convection in deep
748 Mediterranean waters, Ocean Dyn., 75, 46, 2025.

749 van Haren, H., and Dijkstra, H. A.: Convection under internal waves in an alpine lake, Env. Fluid Mech.,
750 21, 305-316, 2021.

751 van Haren, H. and Gostiaux, L.: Detailed internal wave mixing observed above a deep-ocean slope, J.
752 Mar. Res., 70, 173-197, 2012.

753 van Haren, H., and Millot, C.: Seasonality of internal gravity waves kinetic energy spectra in the
754 Ligurian Basin, Oceanol. Acta, 26, 635-644, 2003.

755 [van Haren, H., Millot, C., and I. Taupier-Letage, I.: Fast deep sinking in Mediterranean eddies, Geophys.](#)
756 [Res. Lett., 33, L04606, 2006.](#)

757 van Haren, H., Bakker, R., Witte, Y., Laan, M., and van Heerwaarden, J.: Half a cubic hectometer
758 mooring-array 3D-T of 3000 temperature sensors in the deep sea, J. Atmos. Ocean. Technol.,
759 38, 1585-1597, 2021.

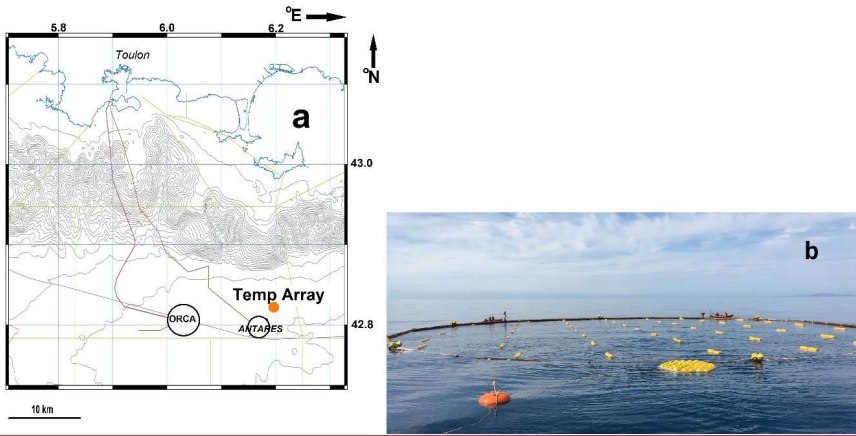
760 van Haren, H., et al.: Whipped and mixed warm clouds in the deep sea, Geophys. Res. Lett., [53,](#)
761 [e2025GL119998](#)~~in press~~, 2026.

762 Yasuda, I., et al.: Estimate of turbulent energy dissipation rate using free-fall and CTD-attached
763 fast-response thermistors in weak ocean turbulence, J. Oceanogr., 77, 17-28, 2021.

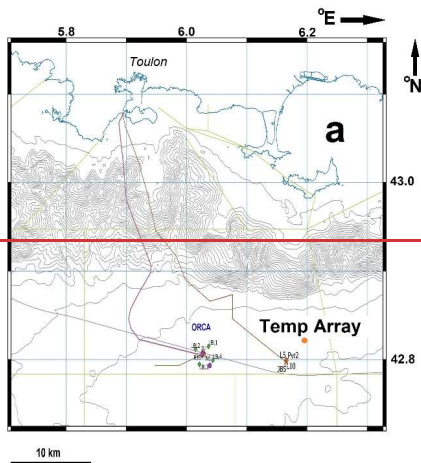
764

765 **Table 1.** General first and second moment statistics calculated for 45-line, 124-m height, and half-day
 766 period turbulence dissipation rate values of Fig. 6. Two environmental conditions are characterized:
 767 SW = stratified-water, NH = near-homogenous, and may include [GH geothermal heating](#). The two
 768 conditions are separated by a criterion equivalent of $N = 0.65f$.

769	<i>Day</i>	$\varepsilon_T [m^2 s^{-3}]$	<i>Cond.</i>
770	308	$4.0 \pm 0.8 \times 10^{-10}$	SW
771	441	$1.5 \pm 0.1 \times 10^{-9}$	SW
772	459	$1.0 \pm 0.2 \times 10^{-10}$	NH
773	495	$1.0 \pm 0.2 \times 10^{-10}$	NH
774	485	$4.8 \pm 0.4 \times 10^{-10}$	SW
775	652	$1.4 \pm 0.1 \times 10^{-10}$	NH
776			
777			



778



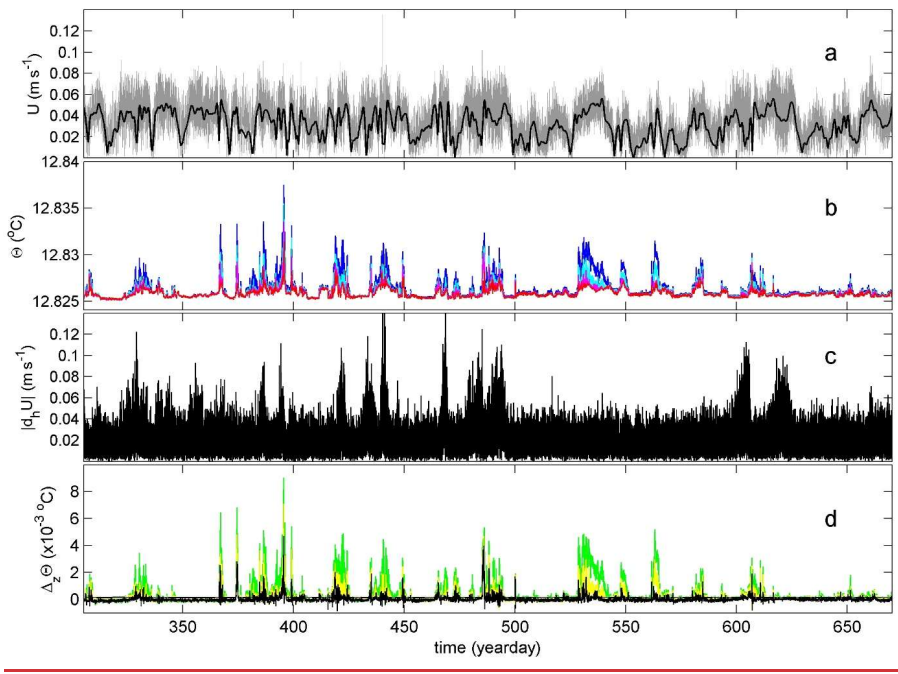
779



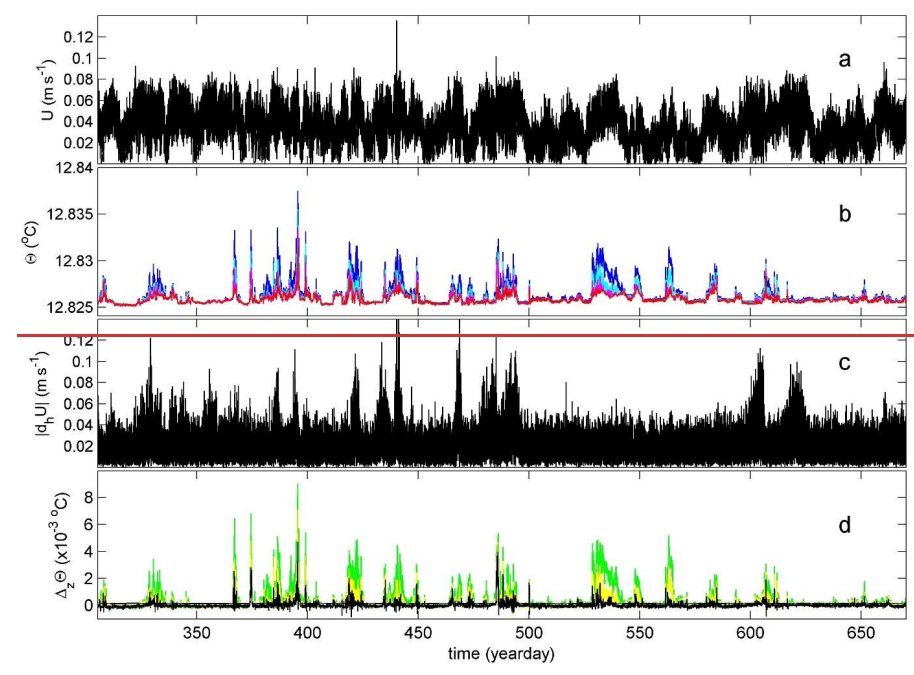
780

781 **Figure 1.** Large-ring mooring site and deployment. (a) Location named "Temp Array" (orange dot) on map
 782 off southern France. The mooring is well east of main neutrino telescope 'NT' site "ORCA" of KM3NeT
 783 (Adrián-Martinez et al., 2016) and just northeast of the former ANTARES NT-site. [Meteorological](#)
 784 [station is at Porquerolles Island, 20 km due North of Temp Array.](#) Isobaths are drawn every 100 m. [The](#)

785 grey lines indicate Toulon-harbour approach sectors. (b) At sea, during deployment finalizing the
786 opening of air valves before sinking. The near part of the large steel-tube ring is already underwater.
787 Almost all buoys of the 45 small-ring compacted vertical lines are visible (for layout see Appendix A1).
788

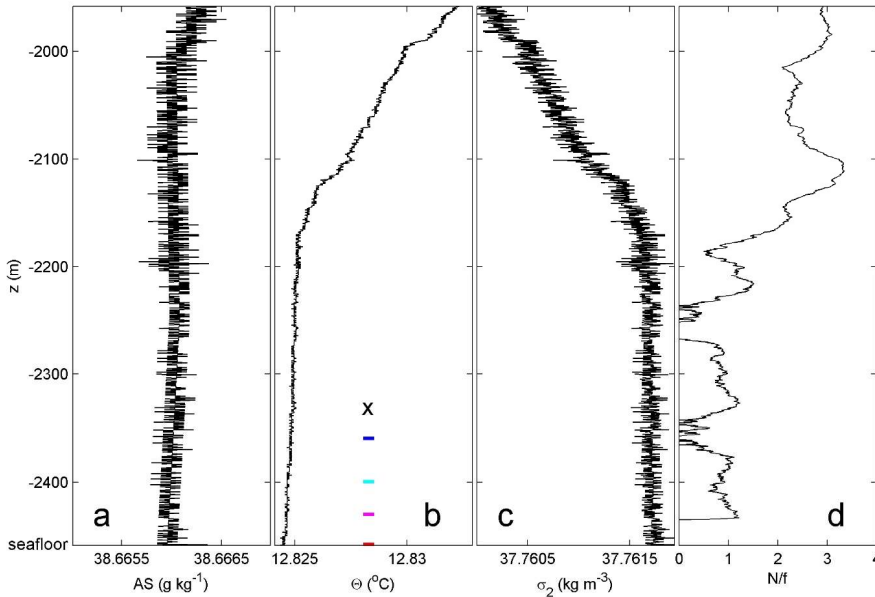


789

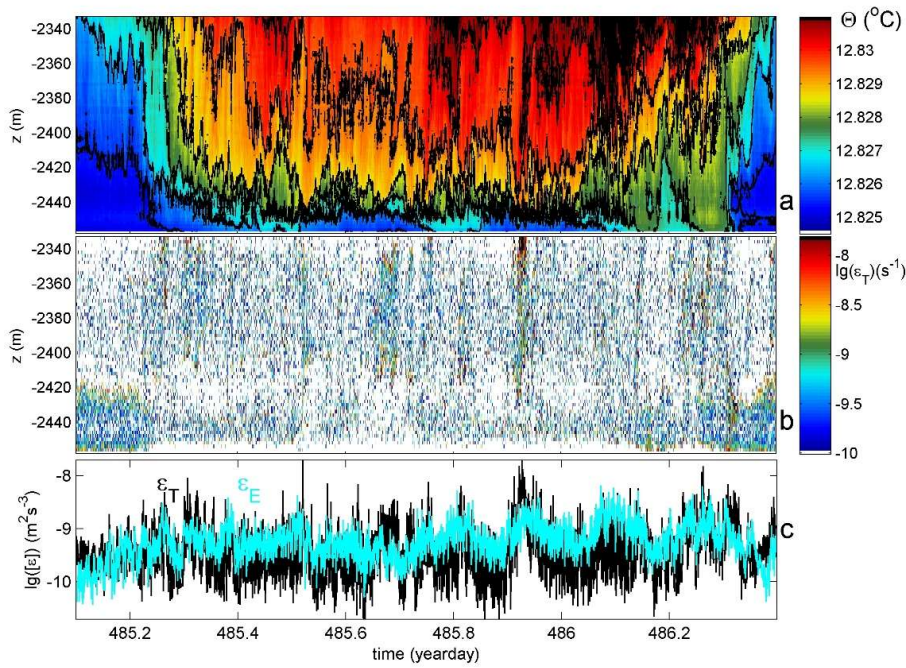


790

791 **Figure 2.** Time series of T-sensor and current meter-^{CM} data, for the first year of sampling data after
 792 deployment. Time in days of year 2020, +366 in 2021. (a) Unfiltered waterflow speed at h = 126 m
 793 above seafloor (grey) and daily filtered (black). (b) Conservative Temperature from vertical line 25,
 794 at h = 1.5 (red), 29.5 (magenta), 59.5 (cyan) and 99.5 m (blue), corrected for drift and referenced to
 795 CTD-data of Fig. 3b. (c) Amplitude of horizontal waterflow differences. (d) Vertical temperature
 796 differences between the lowest T-sensor and those above from b., between 99.5 and 1.5 (green),
 797 between 59.5 and 1.5 m (yellow), between 29.5 and 1.5 m (black).

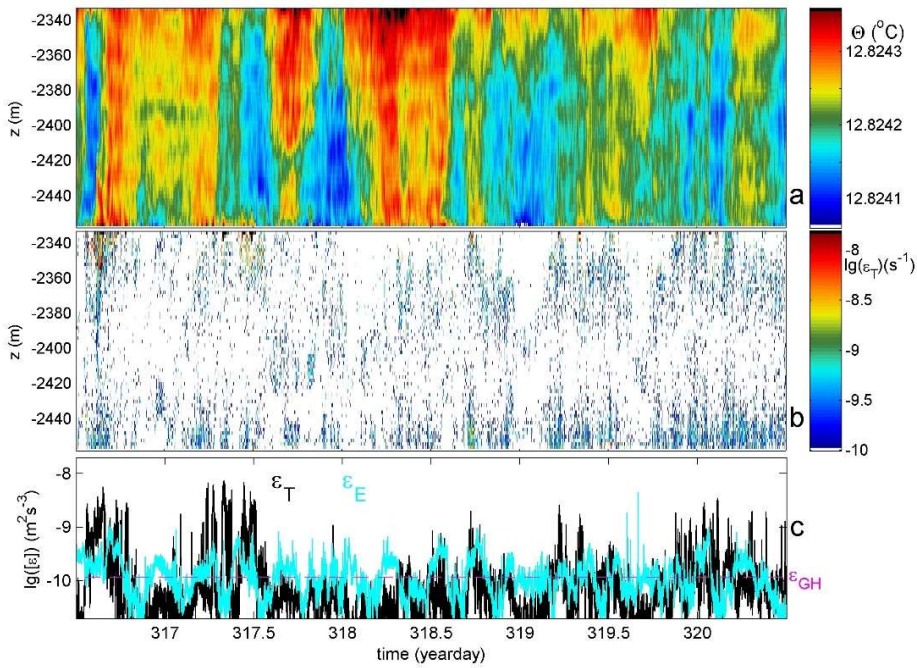


798 **Figure 3.** Lower 500 m of shipborne CTD profile obtained to within 0.5 m from the seafloor (at z = -2458
 799 m). (a) Absolute Salinity, with x-axis range similar to that of b. in terms of contribution to density
 800 variations. (b) Conservative Temperature. The colored ticks indicate the vertical positions of the four T-
 801 sensors of which data are displayed in Fig. 2ba. The 'x' indicates the position of the current meter^{CM}.
 802 (c) Density anomaly referenced to $2 \times 10^7 \text{ N m}^{-2}$. (d) Ratio of 25-m scale buoyancy frequency 'N' over
 803 local inertial frequency 'f'.
 804
 805



806
 807 **Figure 4.** A 1.3-day period of relatively strong stratification with maximum small-scale buoyancy
 808 frequency $N_{\max} = 6f$, for data from vertical line 15. (a) Time-depth plot of Conservative Temperature
 809 with black contours every 0.001°C . The horizontal axis is at the seafloor. (b) Logarithm of non-averaged
 810 turbulence dissipation rate from data in a. using Thorpe (1977) method. (c) Time series of logarithm of
 811 data from b. averaged over 124-m vertical extent of T-sensors (black), compared with calculations using
 812 Ellison (1957) method (cyan) with high-pass filter 'hpf' cut-off from Fig. A2a.

813



814

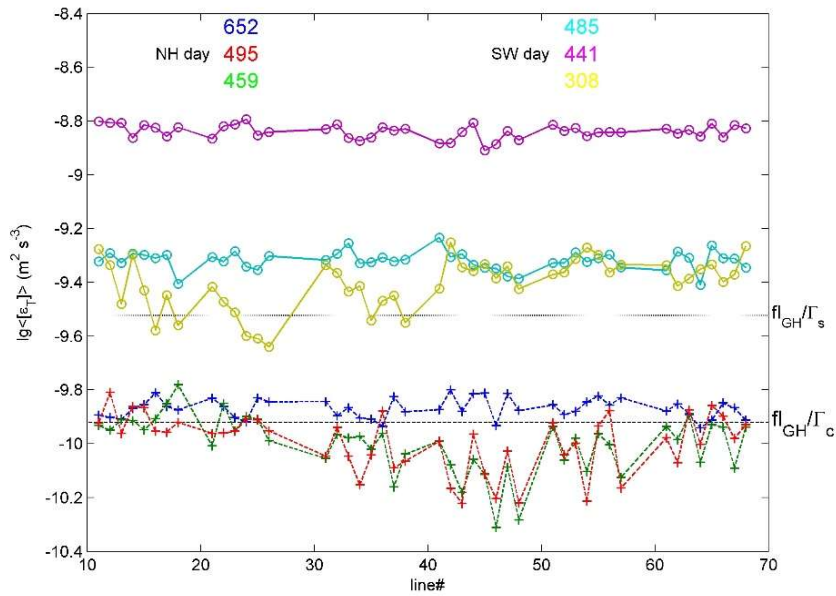
815 **Figure 5.** As Fig. 4, but for four days of near-homogeneous conditions with mean $N \approx 0.5f$, very weak

816 stratification alternated with convectively unstable periods. For c., the hpf cut-off for determining ϵ_E is

817 shown in Fig. A2b and the magenta-dashed line indicates the average turbulence dissipation rate

818 attributed to geothermal heating ϵ_{GH} (see text).

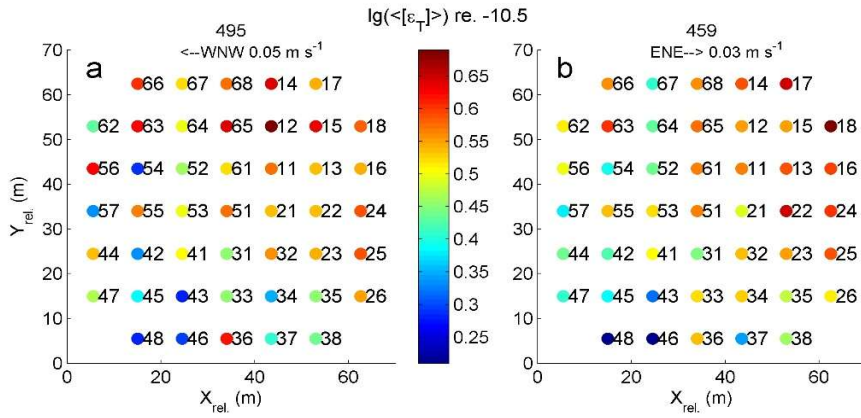
819



820
 821 **Figure 6.** Limited statistics of Thorpe (1977) method (logarithm of) turbulence dissipation rates averaged
 822 over 124 m vertically given for six 12-h periods indicated by day-number, as a function of all 45 lines
 823 that are indicated by their number 'line#'. Two thresholds are given as a function of general average
 824 buoyancy flux ' fl_{GH} ' from GH geothermal heating, divided by mixing coefficient for convection-
 825 turbulence $\Gamma_c = 0.5$ (Dalziel et al., 2008) and for shear-turbulence $\Gamma_s = 0.2$ (Osborn, 1980; Oakey, 1982).
 826 Solid lines (o) indicate Stratified-Water 'SW' conditions, dashed lines (+) indicate Near-
 827 Homogeneous 'NH' conditions.

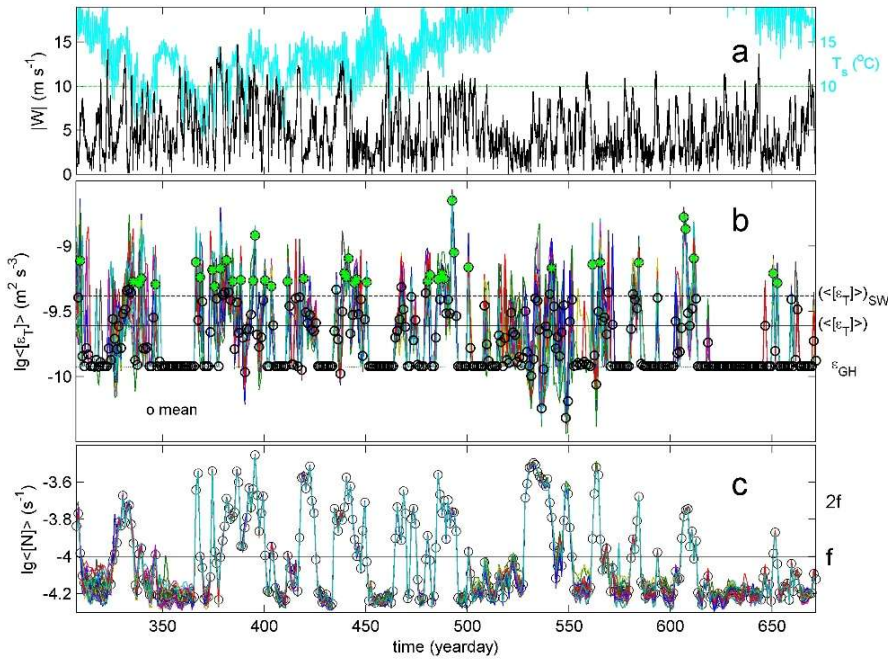
828

Formatted: Subscript



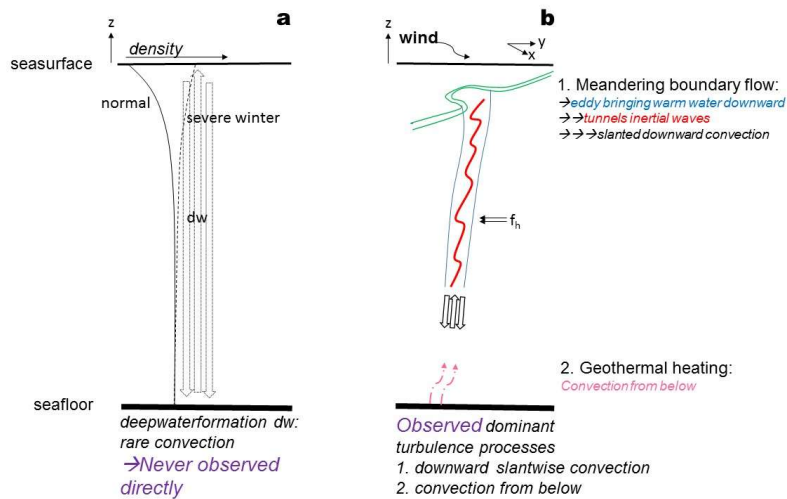
829
 830 **Figure 7.** Plan view of 45 lines indicating logarithm relative to a value of -10.5 of time- and vertical-mean
 831 turbulence dissipation rates underfor NH conditions on days 495 (a) and 4959 (b) of Fig. 6. On top,
 832 half-day mean waterflows are indicated.

833



834
 835 **Figure 8.** Yearlong time series of 45-line, daily, and vertically averaged turbulence dissipation rate and
 836 stratification values compared with meteorological data. (a) Wind speed (black) and surface temperature
 837 (cyan; scale to the right) measured at the station of Porquerolles Island, 20 km north of the mooring-
 838 array. The horizontal line is an arbitrary reference line below which near-surface ocean convection may
 839 occur under sufficient pre-conditioning. (b) Logarithm of daily and 124-m vertically averaged Thorpe
 840 (1977) method turbulence dissipation rate for all 45 lines (colour), including their mean values (black,
 841 circles) of which those exceeding twice the overall mean value (green asterisks). A threshold of 6
 842 0.0002°C is applied for $\Theta_{\text{T}}(h=125\text{ m})-\Theta_{\text{T}}(h=1\text{ m})$, below which values are forced to mean $\epsilon_{\text{GH}} = 1.2 \times 10^{-}$
 843 $10\text{ m}^2\text{ s}^{-3}$, see text. The solid horizontal line indicates the overall mean value (4), the dashed line the mean
 844 (5) for periods under SW conditions. (c) Logarithm of corresponding mean buoyancy frequencies from
 845 reordered temperature profiles. The horizontal line indicates the local planetary inertial frequency.

846



847

848 **Figure 9.** Sketch of potentially relevant flows and turbulence processes in the large-ring mooring area.

849 (a) Rarely occurring, possibly once every 8 years during a severe winter but never directly observed

850 (Thorpe, 2005), convection-turbulence due to deep dense-water formation when the vertical density

851 profile changes from stable (solid graph) to unstable (dashed graph) over the entire 2500-m depth. (b)

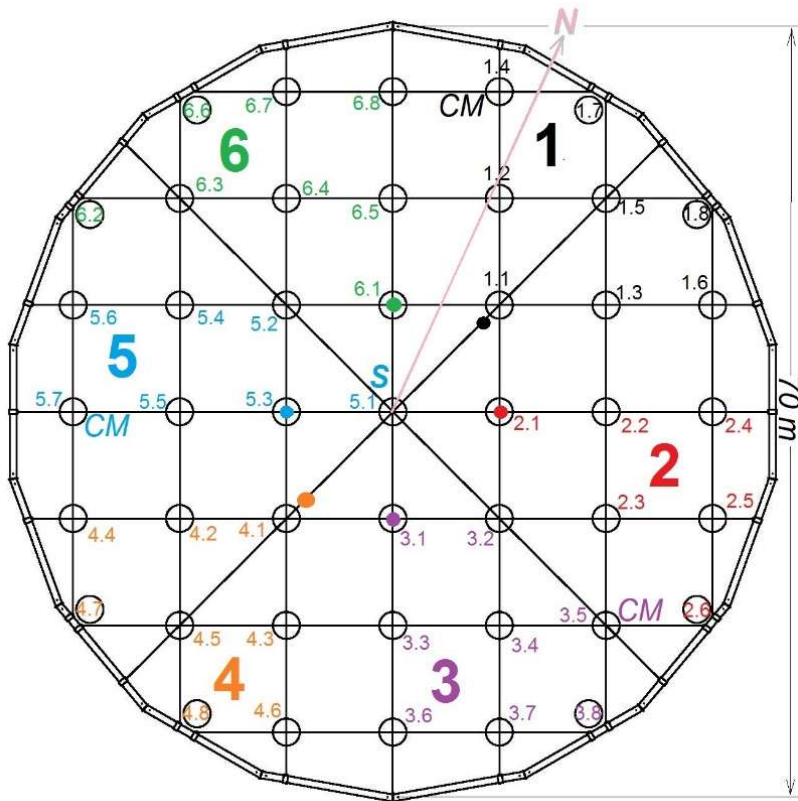
852 Wind-induced boundary flow meandering leading to alternating observations of deep-sea turbulence,

853 from above, via dominant slantwise downward convection, and from below, via geothermal heating.

854 The horizontal Coriolis parameter is indicated by f_h .

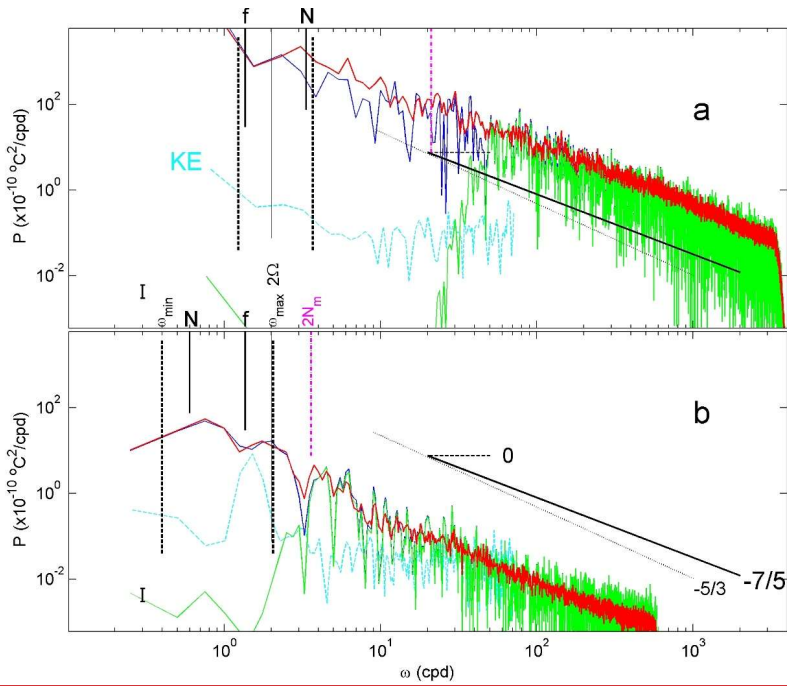
Formatted: Subscript

855

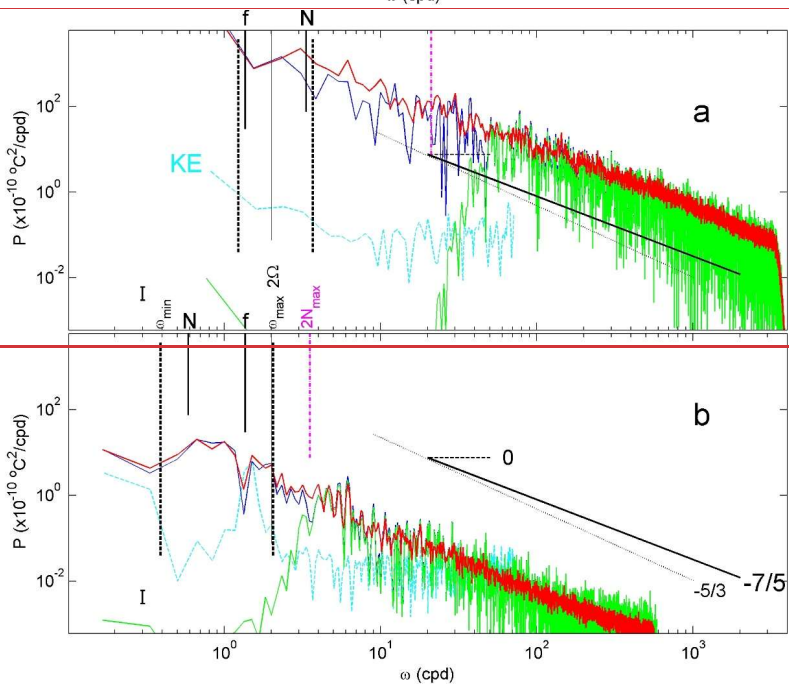


856
 857 **Figure A1.** Orientation and layout of the large-ring mooring viewed from above, with steel-cable grid and
 858 small rings numbered in six synchronisation groups with colour dots indicating group nodes and
 859 synchroniser 'S' at line 51. Here and elsewhere in the text, lines are indicated without period for short.
 860 Lines 14, 35 and 57 held a waterflow current meter 'CM' at the buoy.
 861

862



863



864 **Figure A2.** Spectra demonstrating filter cut-off frequencies for Ellison (1957) method under SW and NH
865 conditions. Data from line 15. Weakly smoothed (6 degrees of freedom, dof) low-pass filtered 'lpf'
866 spectra from a single T-sensor at mid-height (blue) with bhp version (green) is compared with
867 moderately smoothed (100-dof) lpf spectrum over all 63 T-sensors (red). For comparison, the
868 corresponding weakly smoothed (10-dof) kinetic energy 'KE' spectra are given (cyan; arbitrary vertical
869 scale), averaged over the three current meters CM. For reference, several frequencies and turbulence-
870 range spectral slopes are given, see text. (a) SW period of Fig. 4, with filter cut-off following a scaling
871 of time-mean maximum 2-m small-scale buoyancy frequency $\langle N_{max} \rangle^2$ and lpf cut-off at 3000 cpd
872 (cycles per day). (b) NH period of Fig. 5, with hpf cut-off fixed near $2\langle N_{max} \rangle$ and lpf cut-off at 500 cpd.
873